Supplement Information

Synthesis and characterization of $TiO_2/Mg(OH)_2$ composites for catalytic degradation of CWA surrogates

Martin Šťastný*[a,b], Václav Štengl[a], Jiří Henych[a], Jakub Tolasz[a,b], Martin Kormunda[c], Jakub Ederer[b], Gloria Issa[d], and Pavel Janoš[b]

[a]*Institute of Inorganic Chemistry of the Czech Academy of Sciences, 250 68, Řež, Czech Republic*

[b]*Faculty of Environment, University of Jan Evangelista Purkyně in Ústí nad Labem, Králova výšina 3132/7, 400 96 Ústí nad Labem, Czech Republic*

[c]*Faculty of Science, University of Jan Evangelista Purkyně in Ústí nad Labem, České mládeže 8, 400 96 Ústí nad Labem, Czech Republic*

[d]*Institute of Organic Chemistry with Centre of Phytochemistry, Bulgarian Academy of Sciences, Ak. G. Bontchev str., bl.9, 1113, Sofia, Bulgaria*

*corresponding author e-mail: stastny@iic.cas.cz

S1. Synthesis of titania nanoparticles

The thermal hydrolysis of peroxo-complexes was used for titanium(IV) dioxide synthesis.[1,2] In this synthesis route, 30 g of $TiOSO_4$ was dissolved in 100 ml of warm distilled water (produced using a Direct-Q Millipore filtration system with the resistivity of 18.2 MΩ) acidified with 10 ml of 98% H_2SO_4. Once the titanium oxo-sulfate was dissolved in the pellucid solution, NH_4OH solution (10%) in the ratio of 1:1 as a precipitate agent was added under vigorous stirring at the temperature of 0 °C in an ice bath until the reaction mixture reached pH 8.0. The obtained white precipitate $Ti(OH)_4.xH_2O$ was washed by decantation and suspended in 50 mL of 30% hydrogen peroxide (H_2O_2), thereby forming a yellow peroxide titanium phase. The mixture was subsequently heated under reflux for 24 hours, cooled, and washed by decantation, filtered off, and dried at 105 °C.

S2. Synthesis of magnesium hydroxide nanoparticles

The procedure described previously[3] with minor changes was used for the synthesis of $Mg(OH)_2$ nanoparticles. In detail, 26 g of $Mg(NO_3)_2$ was dissolved in 100 mL of hot distilled water (produced using a Direct-Q Millipore filtration system with the *resistivity* of 18.2 MΩ). Subsequently, sodium hydroxide (1M) was added dropwise under vigorous stirring until a milky white suspension of the $Mg(OH)_2$ particles were produced. The suspension was heated at 100 °C for 6 h under stirring, and then the mixture was heated under reflux for 24 hours, cooled, and washed by decantation (to conductivity < 10 μS), then filtered and dried at 105 °C.

S3. Synthesis of TiO_2/$Mg(OH)_2$ composites

For TiO_2/$Mg(OH)_2$ composites, the defined amount of titanium oxo-sulfate $TiOSO_4$ (see **Table S1**) was dissolved in water and hydrolyzed by slow addition of NH_4OH solution (10%) under constant stirring at 0 °C in an ice bath until the reaction mixture reached pH 8.0. Then, the defined amount of $Mg(OH)_2$ prepared by the procedure described above was added, and the whole mixture was washed by decantation and suspended in 50 mL of 30% hydrogen peroxide. The yellow peroxide titanium/$Mg(OH)_2$ mixture was subsequently heated under reflux for 24 hours, cooled, washed by decantation, filtered, and dried at 105 °C. The samples were denoted as TiXXXMgYYY, where XXX and YYY represent the percentage ratio of Ti and Mg. The synthesis route of TiO_2/$Mg(OH)_2$ preparation is shown in **Fig. S1**.

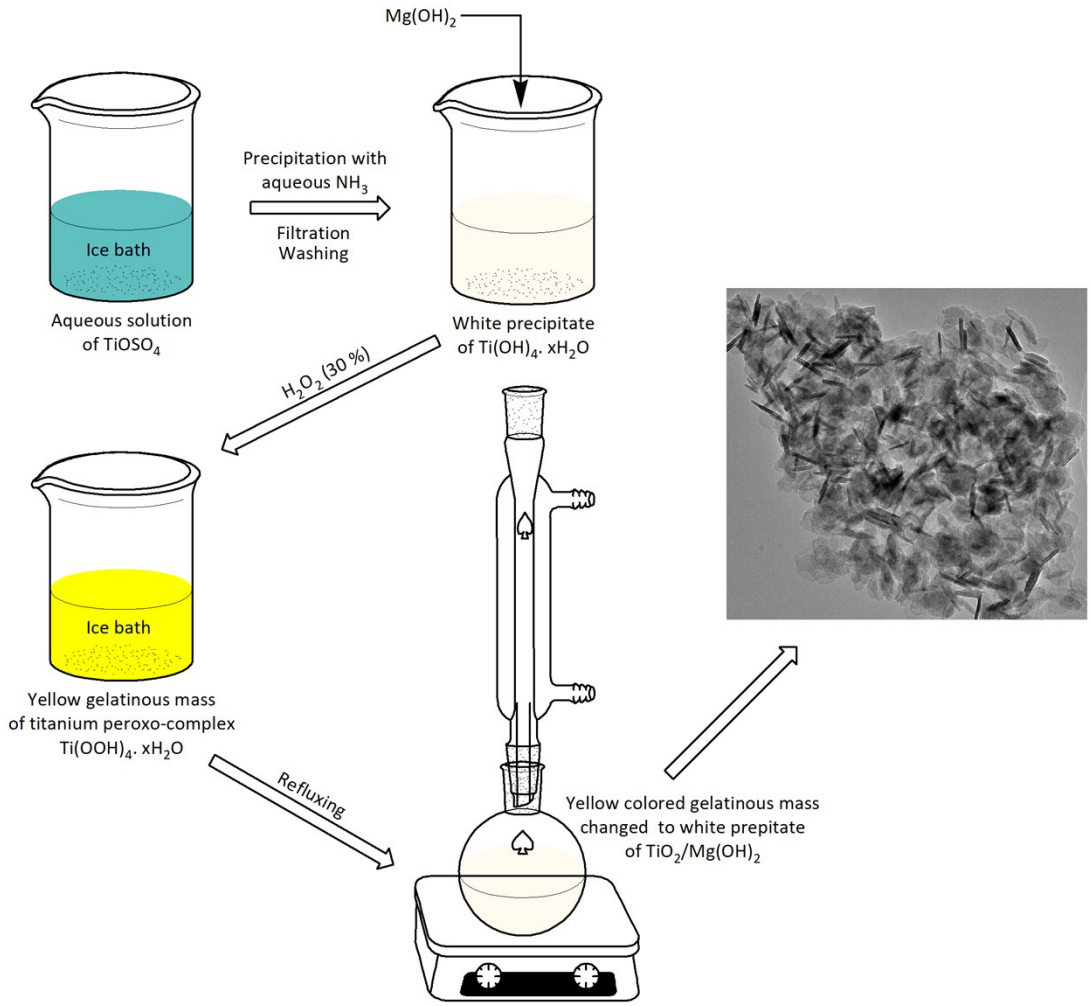

Fig. S1. Scheme of the preparation of $TiO_2/Mg(OH)_2$ catalysts.

S4. X-ray powder diffraction (XRD)

The XRD patterns of the prepared $TiO_2/Mg(OH)_2$ composites are shown in **Fig. S2**. The higher Mg content in the samples (Ti000Mg100 and Ti020Mg080) leads to the formation of crystalline magnesium hydroxide as indicate peaks at 19°, 33°, 38°, 51°, 58°, 62°, 72°, and 81° assigned to brucite phase (JCPDS file No. 96-100-0055). In contrast, the samples with titanium content ≥ 50 at.% (Ti050Mg050, Ti080Mg020 and Ti100Mg000) show only diffractions of anatase phase (JCPDS file No. 96-900-8216) without any traces of brucite. The phase composition, crystallite size, and cell parameters obtained from the Rietveld refinement are shown in **Table S1**.

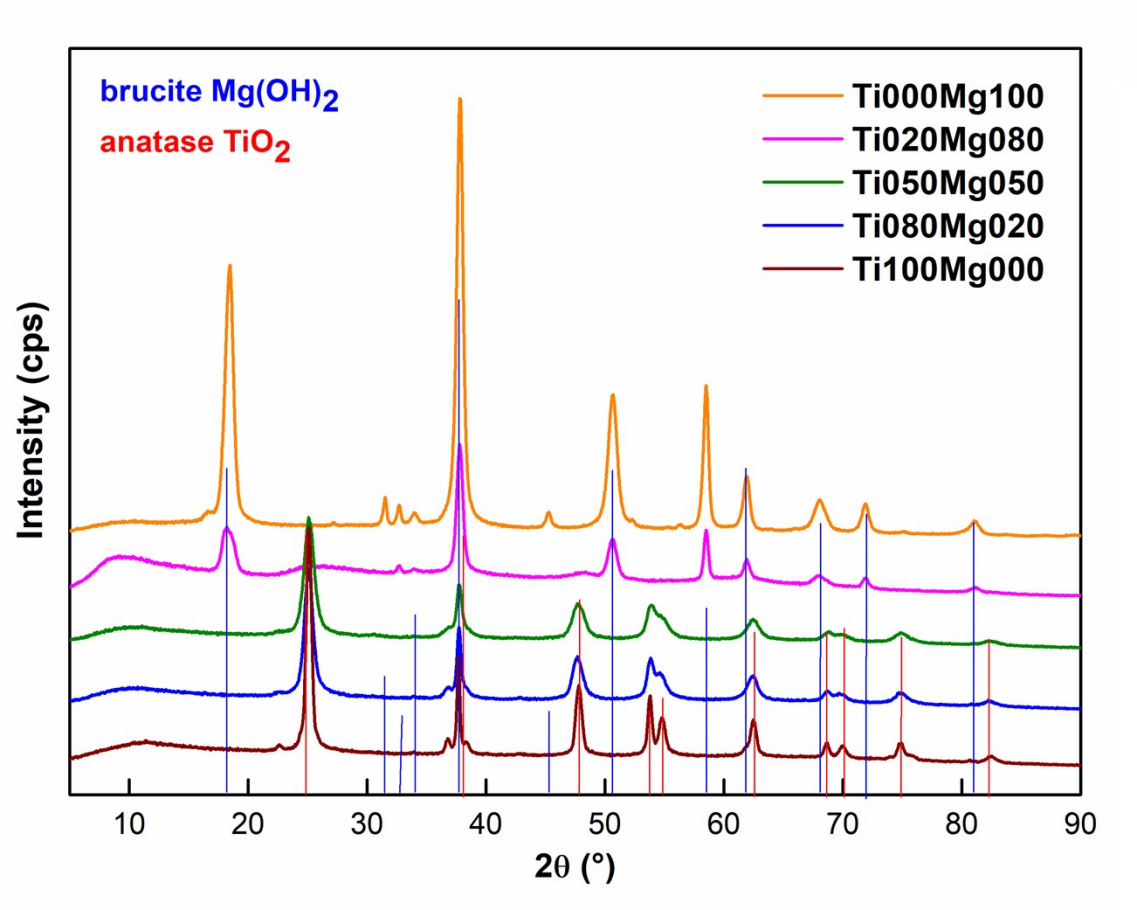

Fig. S2 The XRD patterns of TiO_2/$Mg(OH)_2$ samples.

Table S1. Reaction conditions, phase composition, crystallite size, and cell parameters of the prepared samples.

Sample	$TiOSO_4$ (g)	$Mg(OH)_2$ (g)	TiO_2/$Mg(OH)_2$ (XRD, %)	TiO_2 (Anatase)			$Mg(OH)_2$ (Brucite)		
				Cryst. size (nm)	Cell par. *a* (Å)	Cell par. *c* (Å)	Cryst. size (nm)	Cell par. *a* (Å)	Cell par. *c* (Å)
Ti000Mg100	0.000	25.640	0/100	-	-	-	10.2	9.6	5.7
Ti020Mg080	3.180	20.512	0/100	-	-	-	4.6	14.7	2.5
Ti050Mg050	15.900	25.640	100/0	5.6	6.6	4.7	-	-	-
Ti080Mg020	12.720	5.1280	100/0	9.3	9.6	8.3	-	-	-
Ti100Mg000	30.000	0.0000	100/0	13.1	15.7	2.5	-	-	-

S5. Nitrogen physisorption

To study the adsorption capacity of $TiO_2/Mg(OH)_2$ catalysts, we studied the surface properties like BET surface area, pore-volume, and pore size of the composites using nitrogen adsorption-desorption analysis (see **Table S2**).

As can be seen from **Table S2**, the surface area (A_{BET}) and total pore volume (V_{tot}) of the samples obtained from nitrogen physisorption differ substantially between pure (hydr)oxides and $TiO_2/Mg(OH)_2$ composites. Pure magnesium hydroxide (Ti000Mg100) had the lowest surface area (105 $m^2 \cdot g^{-1}$) and V_{tot} = 0.33 $cm^3 \cdot g^{-1}$. Pure titanium dioxide (Ti100Mg000) possessed slightly higher surface area 116 $m^2 \cdot g^{-1}$ and almost the same pore volume 0.35 $cm^3 \cdot g^{-1}$. Surprisingly, in the $TiO_2/Mg(OH)_2$ composites increasing amount of Ti leads to a gradual increase in the surface area. The pore volume does not depend on the Ti content; however, the highest pore volume (V_{tot} = 0.40 $cm^3 \cdot g^{-1}$) was observed for composite with the highest of Ti (Ti080Mg020), which also had the highest A_{BET} = 223 $m^2 \cdot g^{-1}$. In addition, increasing the amount of Ti leads to a change in the shape of the isotherm hysteresis. N_2 adsorption-desorption analysis indicates the nature of the curves are of Type IV isotherm (see the inset of **Fig. S3**), the characteristic feature of which is Type H3 hysteresis loop associated with capillary condensation taking place in the mesopores due to aggregates of plate-like $Mg(OH)_2$ nanoparticles in pure Mg sample (Ti000Mg100) and composite with the highest amount of Mg (Ti020Mg080). The gradual increase of Ti in samples changed the hysteresis loop from H3 hysteresis of magnesia[4] to H2 hysteresis of titania[5] with a type IV isotherm, which is characteristic of large-pore mesoporous materials with capillary pores, wide ink-bottle pores, and wedge-shaped capillaries[6]. The pore size distribution calculation based on the Barrett–Joyner–Halenda (BJH) method using the adsorption branch of isotherm is shown in **Fig. S3**. While pure titania and magnesia had larger pores in range ca 8–15 nm, the mixing of TiO_2 with $Mg(OH)_2$ led to a significant change in the pore distribution and amount of adsorbed gas. The sample with the Ti/Mg ratio of 50/50 (Ti050Mg050) showed a very narrow pore distribution (<5 nm). Very low gas adsorption was observed for the sample with 20at% of titania (Ti020Mg080).

Table S2. The elemental composition obtained from TEM/EDS mapping, specific surface area (A_{BET}), and total pore volume (V_{tot}) of the prepared samples.

Sample	Element		A_{BET} ($m^2 \cdot g^{-1}$)	V_{tot} ($cm^3 \cdot g^{-1}$)
	Ti (at. %)	Mg (at. %)		
Ti000Mg100	-	94.7	105	0.33
Ti020Mg080	54.4	45.6	154	0.24
Ti050Mg050	64.4	35.6	177	0.13
Ti080Mg020	95.7	4.3	223	0.40
Ti100Mg000	93.5	-	116	0.35

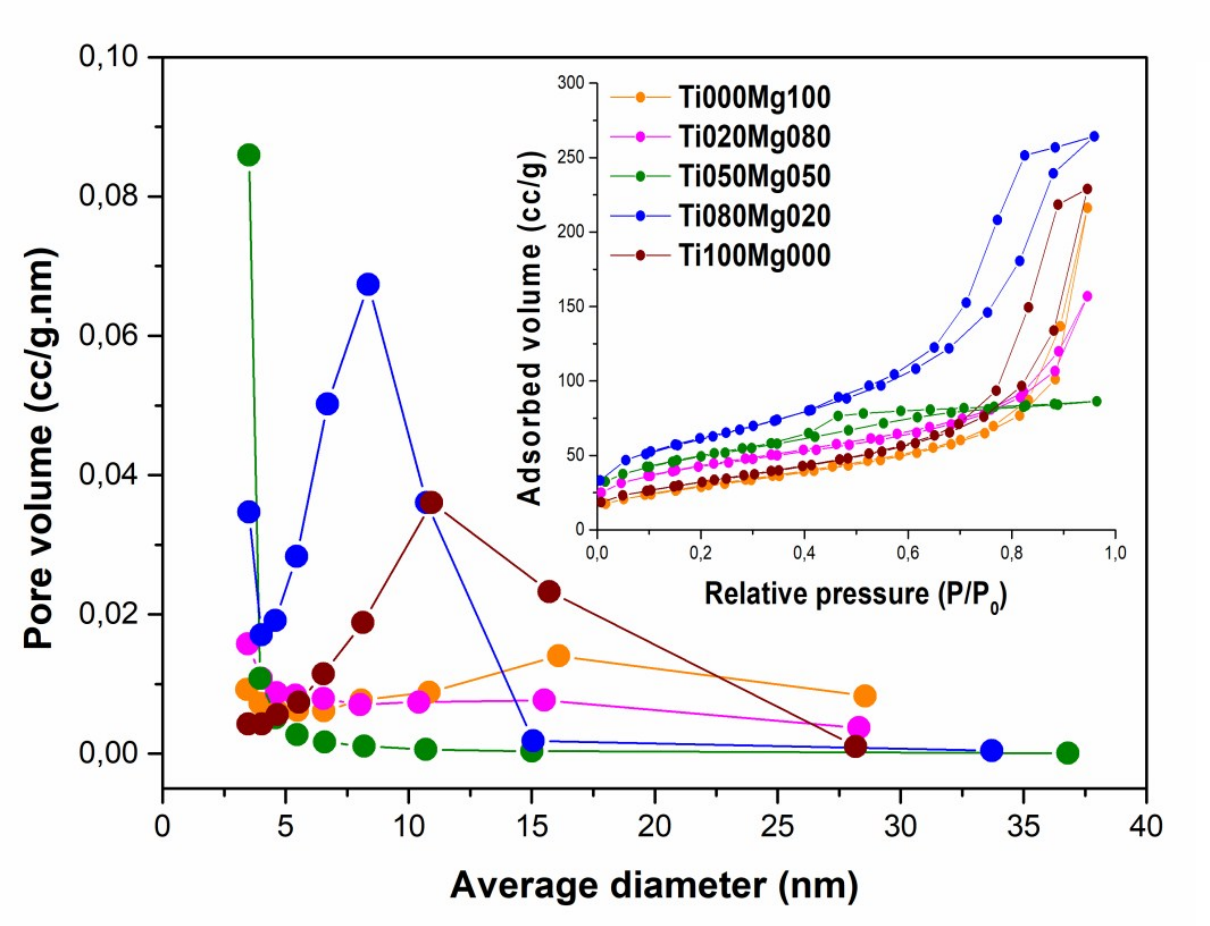

Fig. S3. The pore size distribution and isotherm (inset) of $TiO_2/Mg(OH)_2$ samples.

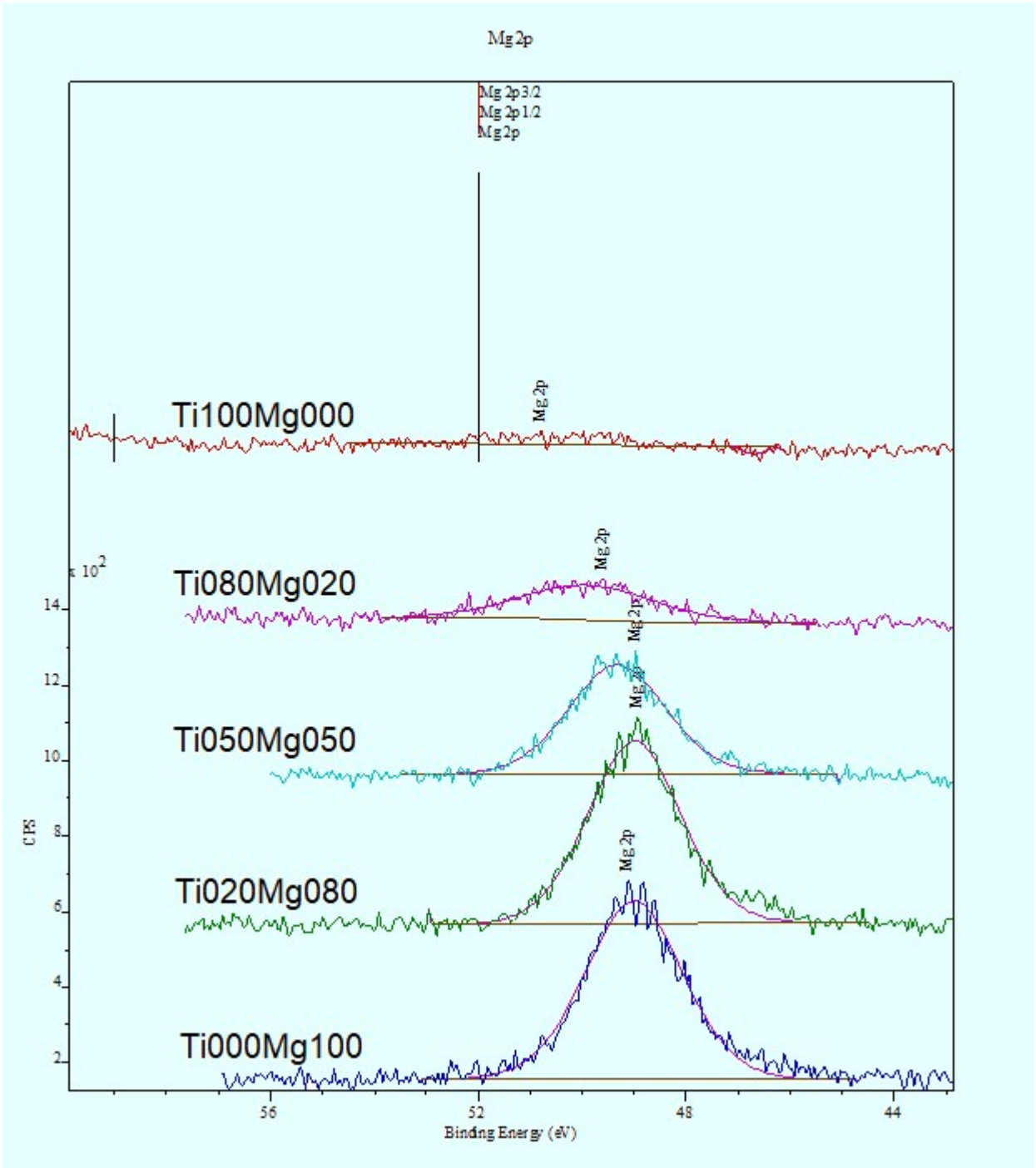

Fig. S4. The high-resolution spectra Mg 2p from up TiO_2 (Ti100Mg000) to $Mg(OH)_2$ (Ti000Mg100) down.

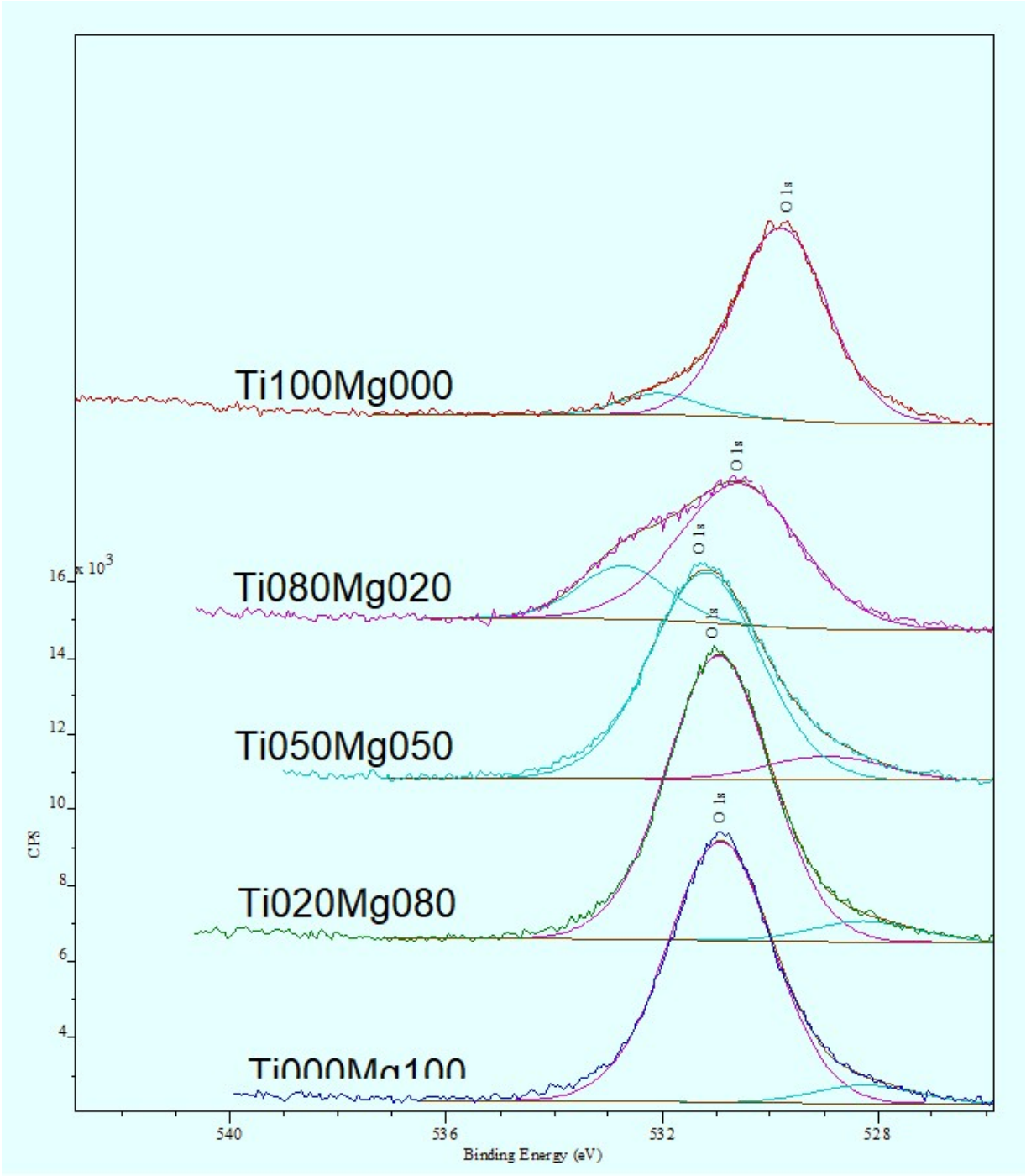

Fig. S5. The high-resolution spectra O 1s from up TiO_2 (Ti100Mg000) to $Mg(OH)_2$ (Ti000Mg100) down.

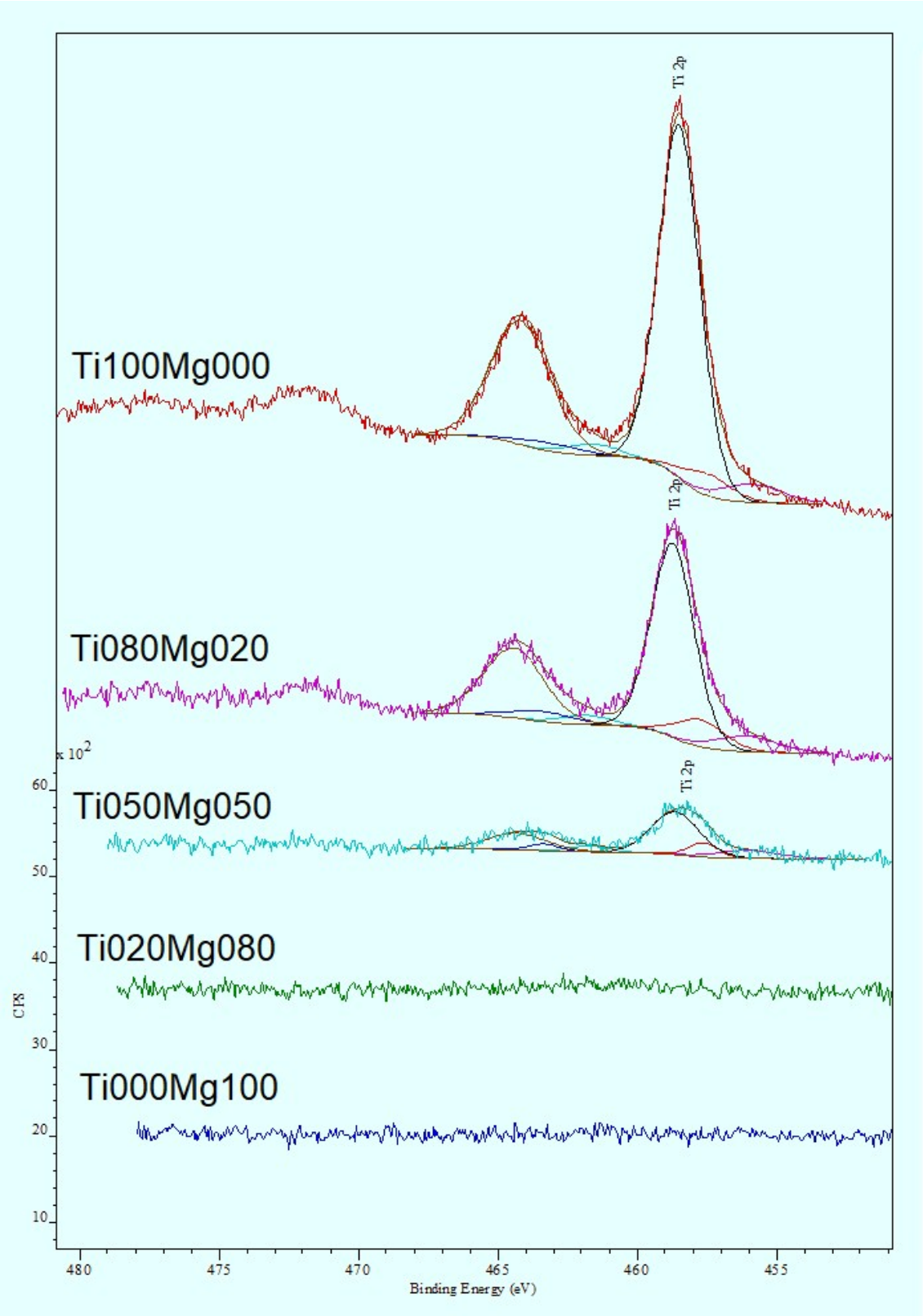

Fig. S6. The high resolution spectra Ti 2p from up TiO_2 (Ti100Mg000) to $Mg(OH)_2$ (Ti000Mg100) down.

Table S4. XPS surface elemental composition (at. %) of the prepared samples.

Sample	C	Mg	O	Ti
	[at. %]	[at. %]	[at. %]	[at. %]
Ti100Mg000	13.6	-	62.4	24.0
Ti080Mg020	9.9	4.4	62.3	23.5
Ti050Mg050	10.3	16.8	59.3	13.6
Ti020Mg080	7.4	32.5	56.7	3.4
Ti000Mg100	7.0	36.1	56.9	-

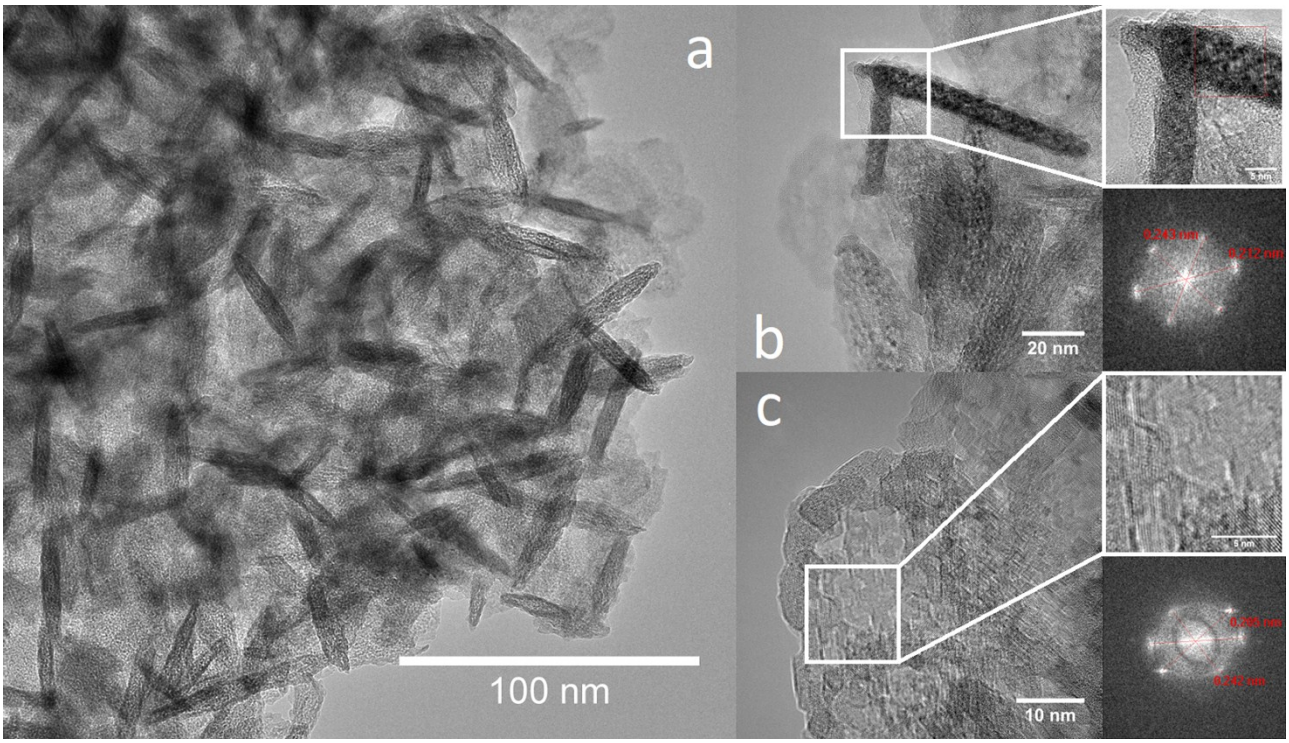

Fig. S7. TEM (a) and HRTEM (b) micrographs of the Ti020Mg080 sample. Insets give a magnification of selected areas and appropriate FFR patterns.

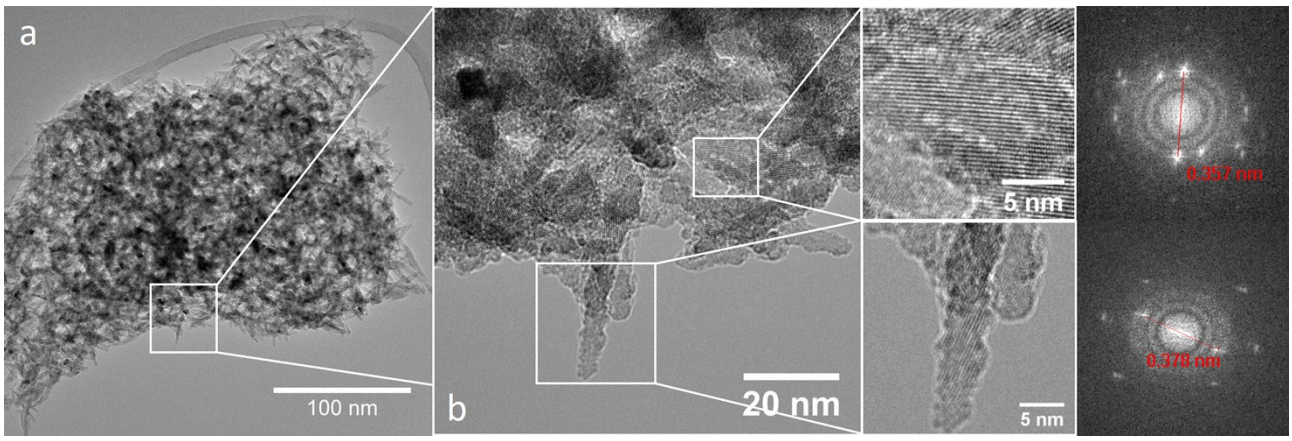

Fig. S8. TEM (a) and HRTEM (b) micrographs of the Ti080Mg020 sample. Insets give a magnification of selected areas and appropriate FFR patterns.

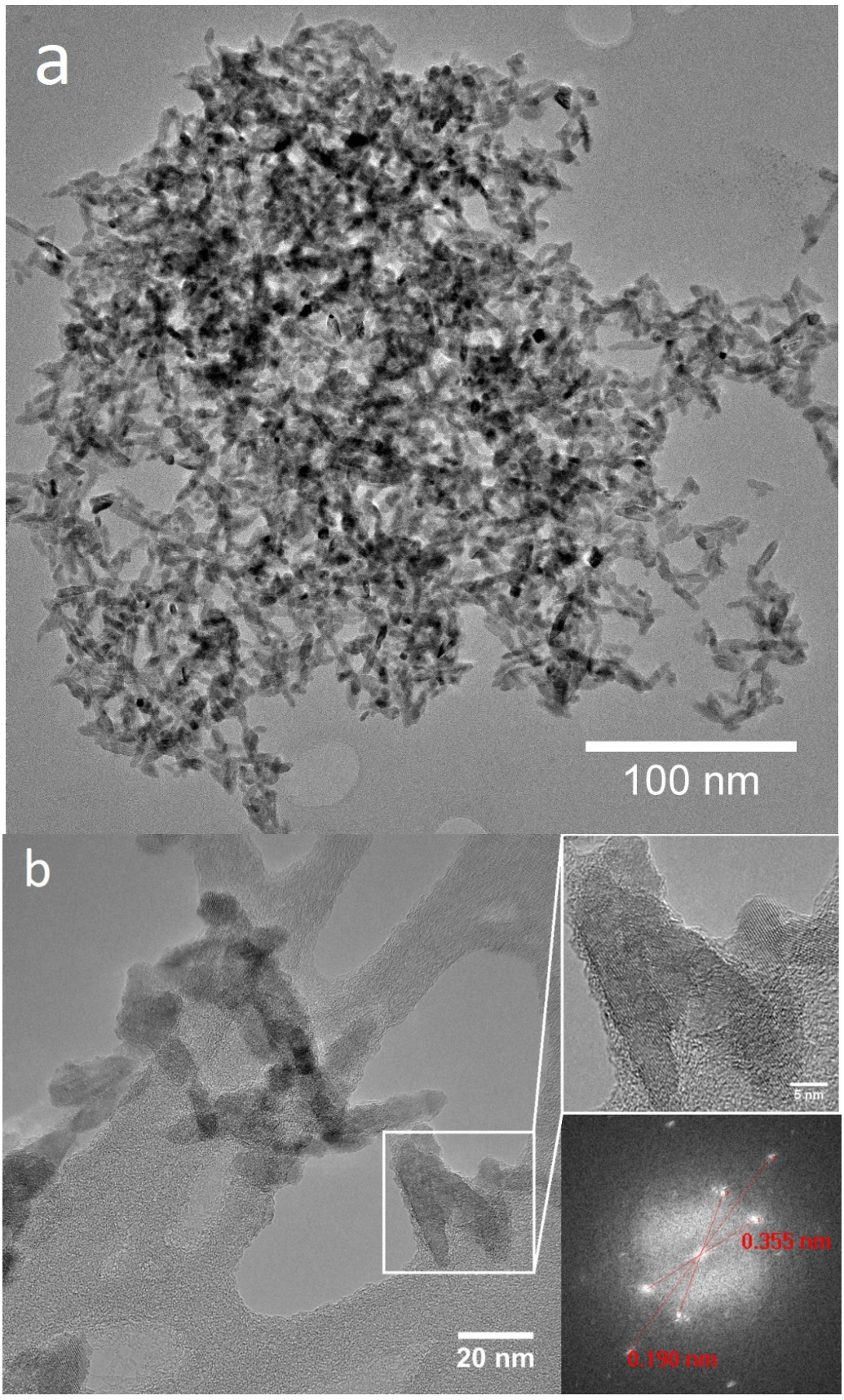

Fig. S9. TEM (a) and HRTEM (b) micrographs of the Ti100Mg000 sample. Insets give a magnification of selected areas and appropriate FFR pattern.

Table S5. Kinetic parameters for the reactive adsorption of CWA surrogates 2-CEES and 2-CEPS in the water on the surface of the sample denoted Ti050Mg050.

CWA surrogate	Pseudo-first order kinetic parameters			Qualitative parameters	
	$k \pm SE$[a)] (min^{-1})	$\tau_{1/2}$[b)] (min)	d[c)] (%·120 min^{-1})	[d)]R^2	SEE[e)]
2-CEES	0.115 ± 0.002	6.0	79.5	0.9895	0.001
2-CEPS	0.047 ± 0.003	14.7	92.2	0.9875	0.001

[a)]SE is the standard error of the estimated parameter; [b)]$\tau_{1/2}$ is the half-life time of the decaying quantity of CWA surrogate (min); [c)]d is the degree of conversion of CWA surrogate after 120 minutes (%); [d)]R^2 is the determination coefficient obtained by fit; [e)]SEE is the standard error of the estimate

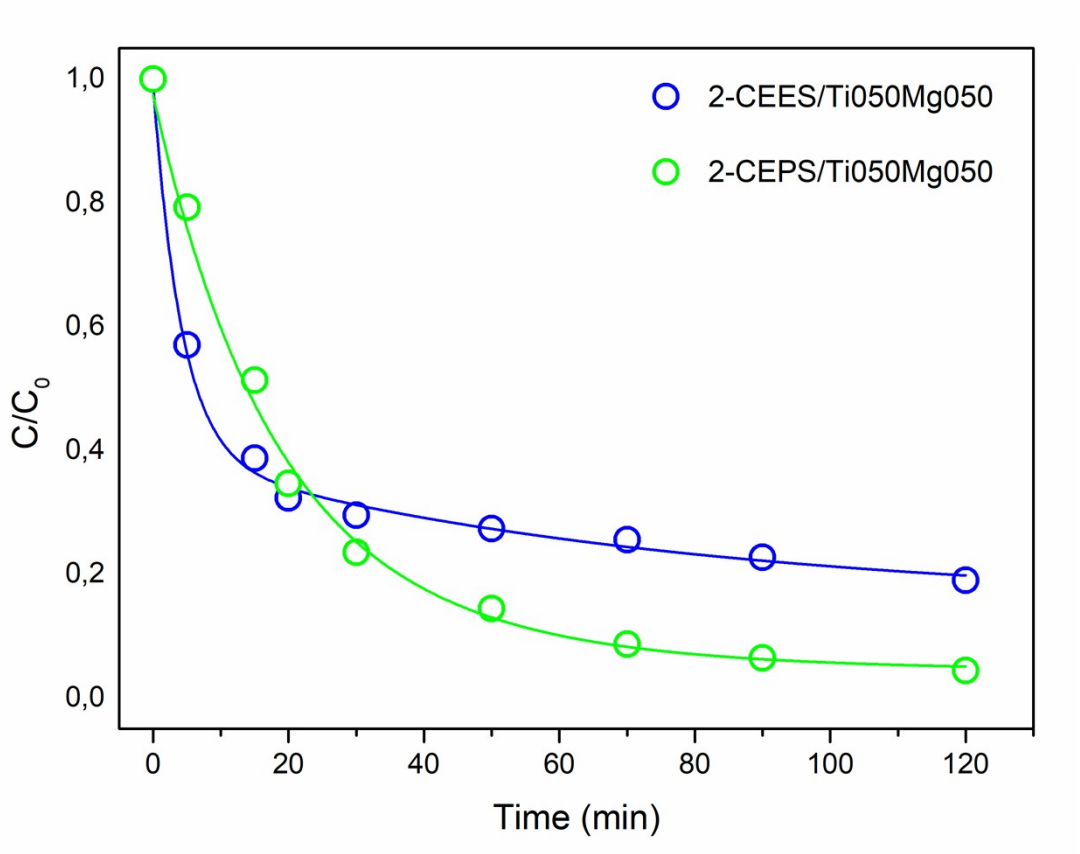

Fig. S10. Normalized kinetic curves for the degradation of CWA surrogates 2-CEES and 2-CEPS in the water on the surface of the sample denoted Ti050Mg050.

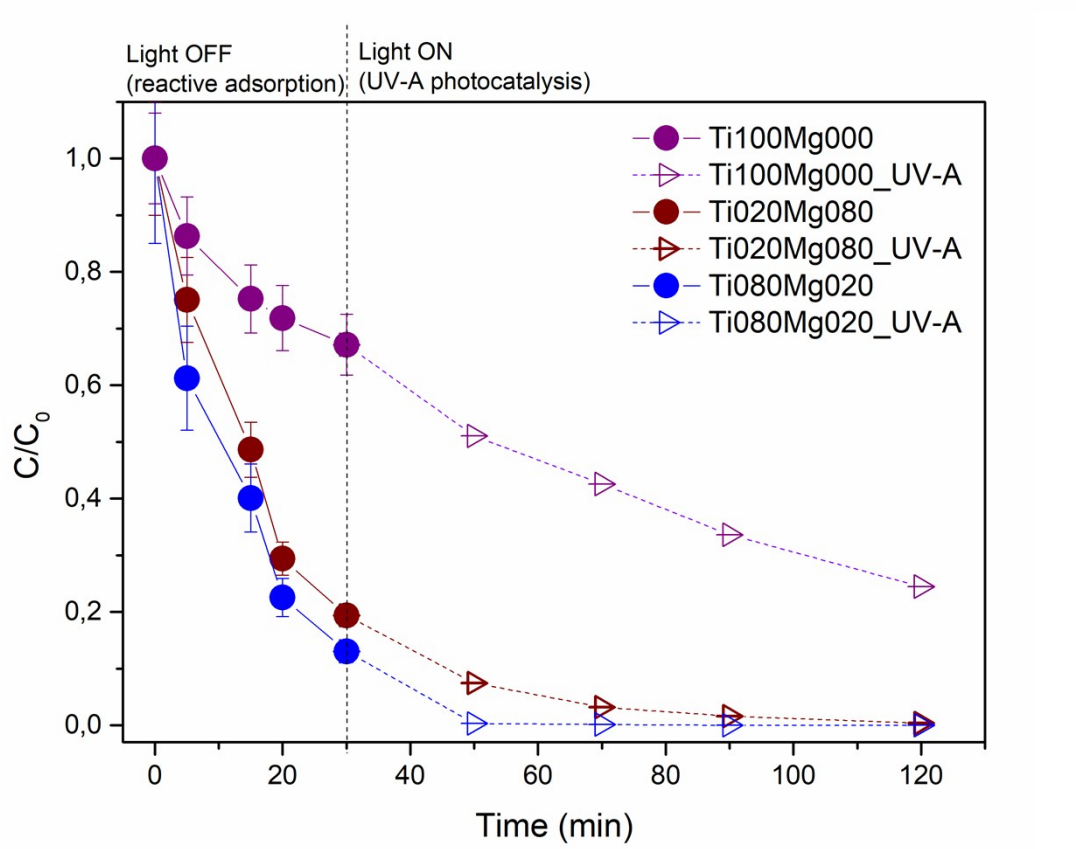

Fig. S11. Normalized kinetic curves for the UV-A photocatalytic degradation of DMMP surrogate in the water on the surface of samples denoted Ti100Mg000 (pure titania), Ti020Mg080, and Ti080Mg020.

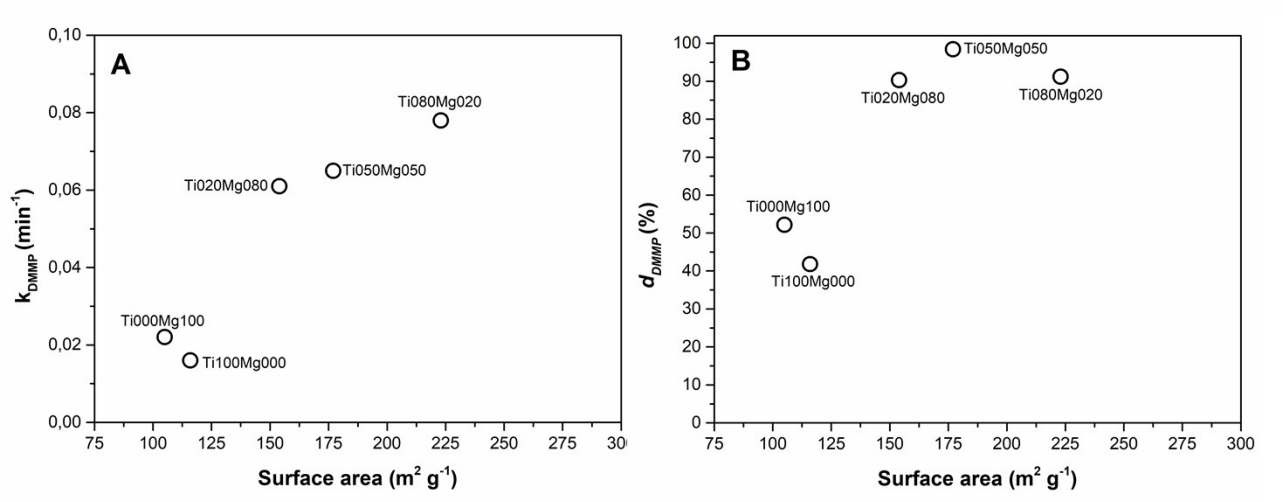

Fig. S12. Graphs of dependence: The rate constant of the DMMP decomposition on surface area (A) and degree of conversion after 120 min on surface area (B).

Gas chromatograms and Electron-ionization (EI) mass spectra of CWA surrogates

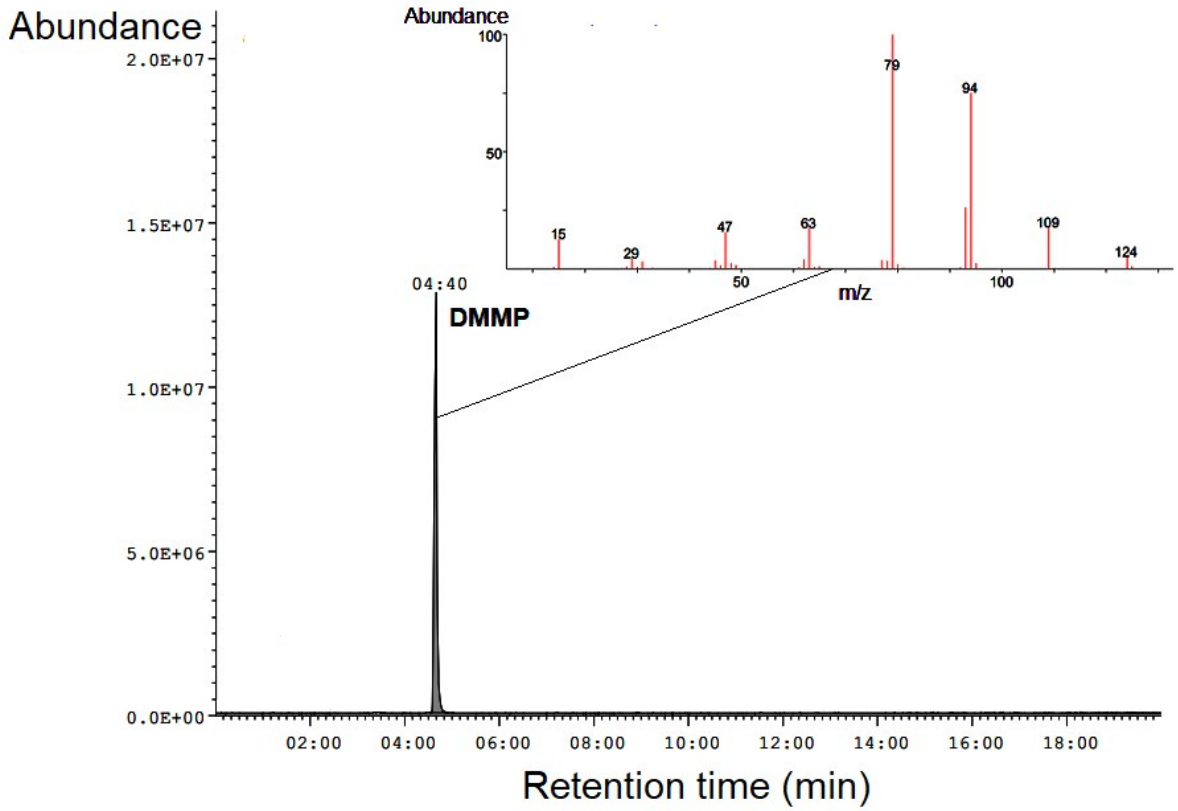

Fig. S13. GC chromatogram of DMMP and its mass spectrum.

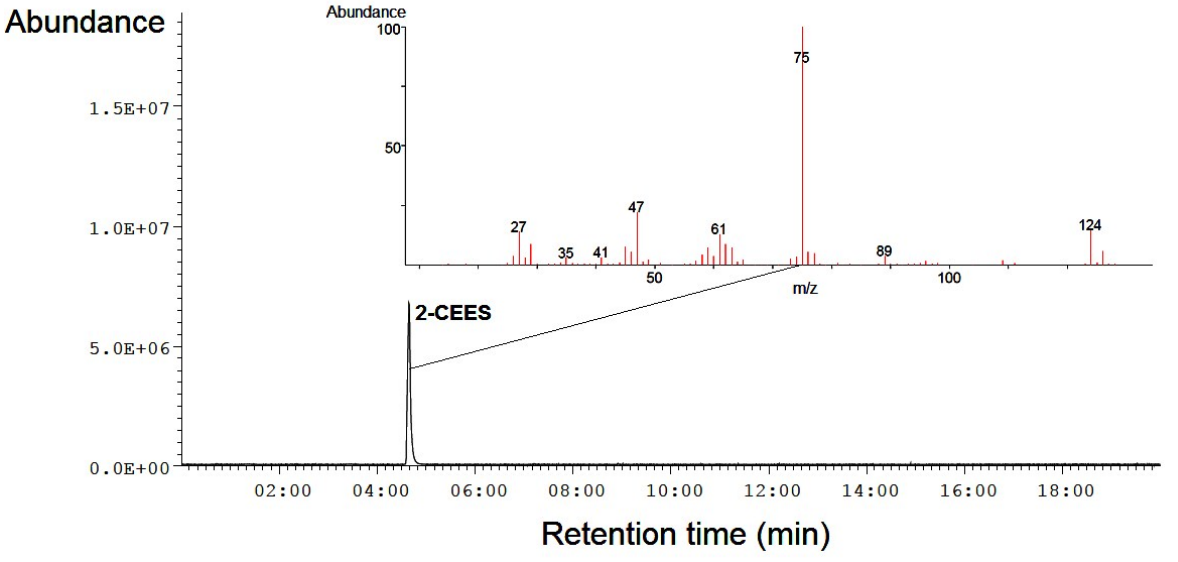

Fig. S14. GC chromatogram of 2-CEES and its mass spectrum.

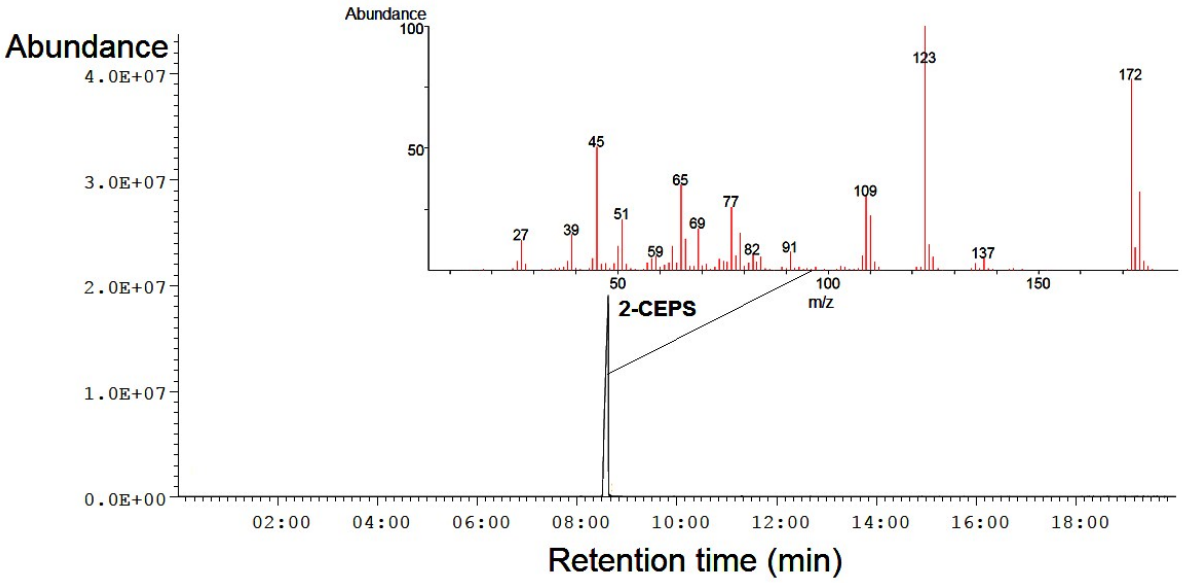

Fig. S15. GC chromatogram of 2-CEPS and its mass spectrum.

References

1 V. Štengl, V. Houšková, S. Bakardjieva, N. Murafa and P. Bezdička, *J. Mater. Res.*, , DOI:10.1557/jmr.2010.0252.

2 V. Štengl and T. M. Grygar, *Int. J. Photoenergy*, , DOI:10.1155/2011/685935.

3 B. Nazari and M. Jaafari, *Dig. J. Nanomater. Biostructures*.

4 J. Zhou, W. Wang, Y. Cheng and Z. Zhang, *Integr. Ferroelectr.*, , DOI:10.1080/10584587.2012.687251.

5 V. Stengl, T. Matys Grygar, J. Henych and M. Kormunda, *Chem. Cent. J.*, 2012, **6**, 113.

6 K. A. Cychosz and M. Thommes, *Engineering*, 2018.